**Showcasing research from Nanyang Technological University, Singapore, and Ningxia University, China.**

Bismuth–nickel bimetal nanosheets with porous structure for efficient hydrogen production in neutral and alkaline media

A Bi–Ni alloy nanosheet with porous structure has been prepared, which exhibits enhanced activity and durability to electrocatalytic hydrogen evolution reaction.

As featured in:
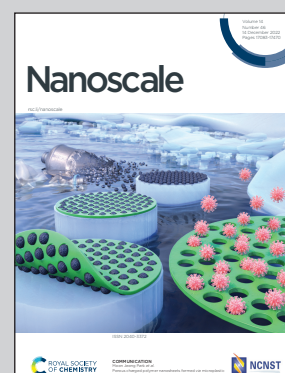
ROYAL SOCIETY
OF **CHEMISTRY**

rsc.li/nanoscale

Bismuth–nickel bimetal nanosheets with a porous structure for efficient hydrogen production in neutral and alkaline media†

Xueping Yu,‡[a] Li Qu,‡[a] Carmen Lee,[b] Juan Peng, ✶[a] Qingyu Yan, ✶[b,c] Hongcun Bai[a] and Min Yao[a]

Active and durable electrocatalysts are very important for efficient and economically sustainable hydrogen generation *via* electrocatalytic water splitting. A bismuth–nickel (Bi–Ni) bimetal nanosheet with a meso-porous structure was prepared *via* a self-template electrochemical *in situ* process. The Bi–Ni catalyst required overpotentials of 56 mV and 183 mV at 10 mA cm^{-2} for the hydrogen evolution reaction (HER), which were close to that of commercial Pt/C in 1.0 M KOH and 1.0 M PBS (pH 7.0), respectively. The electrocatalyst maintained a steady current density during 20 h electrolysis in 1.0 M KOH and 1.0 M PBS (pH 7.0). Density functional theory (DFT) indicated that the alloying effect could induce charge transfer from the Bi atom to Ni atom and thus modulate the d-band centre of Bi–Ni nanosheets, which could efficiently accelerate H* conversion and H$_2$ desorption at the Ni active site. This promotes the HER kinetics. By adopting the Bi$_{84.8}$Ni$_{15.2}$ alloy as the cathode to establish a full-cell (IrO$_2$‖Bi$_{84.8}$Ni$_{15.2}$) for water splitting in 1.0 M KOH, the required cell voltage was 1.53 V to drive 10 mA cm^{-2}, which was lower than that of the IrO$_2$‖Pt/C electrolyzer (1.64 V@10 mA cm^{-2}).

1. Introduction

Due to its high energy density and environmentally friendly characteristics, hydrogen is an attractive and promising renewable energy substitute for fossil fuels.[1] At present, most industrial hydrogen-generation methods are heavily reliant on fossil fuels, resulting in a large amount of CO$_2$ emissions.[2] Electrochemical water splitting stands out from the various hydrogen production strategies because it is clean, efficient, and can be coupled with renewable energy sources (solar, wind, *etc.*).[3,4] Nowadays, electrochemical water splitting in an alkaline condition can meet the needs of industrial hydrogen production. Water electrolysis in a neutral electrolyte can potentially enable the direct usage of saltwater without the requirement for desalination.[5] Additionally, the neutral hydrogen evolution reaction

(HER) can also be combined with bio-processes for the production of solar fuels.[6] However, the HER has sluggish reaction kinetics in alkaline and neutral circumstances, due to the high activation barrier for the dissociation of H$_2$O molecules and the formation of H* (H$_2$O + e$^-$ = H* + OH$^-$).[7] Therefore, it is meaningful to design HER electrocatalysts with high catalytic performance in both neutral and alkaline conditions.

Bismuth nanosheets with a 2D nanostructure have been widely used in the field of electrocatalysis because of their unique physical characteristics.[8] Norskov *et al.* predicted and verified that alloying bismuth with a noble metal (such as Pt) can effectively reduce ΔG_{H*} and enhance the HER activity in acidic media, and that its activity is even better than that of platinum catalysts.[9] However, the alloy includes a noble metal and is only used for acidic HER. Nowadays, although Pt is the most widely used catalyst in a pH-universal range, its high-cost and scarcity limit its scalable application.[10,11] Therefore, it is necessary and challenging to design and develop bismuth-based non-noble metal catalysts with a wide pH range for HER. Alloying with a metal element in monophase catalysts can effectively tune the electronic structures and optimize the intermediates absorption energy of materials in HER or OER, and thus substantially improve the intrinsic catalytic properties.[12–14] Notably, Ni atoms are broadly recognized as excellent water dissociation centres.[15] Ni alloying/doping can play a role in strengthening the electrocatalytic activity and

[a]*College of Chemistry and Chemical Engineering, State Key Laboratory of High-efficiency Utilization of Coal and Green Chemical Engineering, Ningxia University, Yinchuan 750021, P. R. China. E-mail: pengjuan@nxu.edu.cn*
[b]*Center for Programmable Materials, School of Materials Science and Engineering, Nanyang Technological University, Singapore 639798, Singapore.*
E-mail: alexyan@ntu.edu.sg
[c]*Institute of Materials Research and Engineering, A*STAR, 2 Fusionopolis Way, Innovis, #08-03, Singapore 138634, Singapore*
†Electronic supplementary information (ESI) available. See DOI: https://doi.org/10.1039/d2nr04407b
‡These authors contributed equally to the manuscript.

improving the catalytic efficiency of Ni-based catalysts by adjusting the electronic structure of the alloy's surface.[15–19] Additionally, 2D porous structures feature a large surface area, abundant active sites,[20,21] excellent gas-diffusion capacity and rapid electrode kinetics in the HER process.[22,23] Most 2D porous electrocatalysts are prepared using porous templates[24] or substrates.[25,26] Nevertheless, 2D porous nanomaterials are still very rare as it is difficult to form pores directly in 2D nanostructures without a template or porous substrate.[27]

Herein, we demonstrate a simple self-templating strategy for the synthesis of 2D mesoporous Bi–Ni alloy *via* an electrochemical *in situ* process without using any template or substrate. Density functional theory (DFT) results suggested that the strong interaction between the surface Ni sites and OH, and between the Bi sites and H cause a breakage of the H–OH bonds (Volmer step: $H_2O + e^- = H^* + OH^-$) to facilitate H* formation. Subsequently, the adjacent surface Ni atoms exhibit a suitable H*-binding ability, which accelerates the H* conversion and H_2 desorption (Heyrovsky step: $H_2O + e^- + H^* = H_2 + OH^-$). This would improve the overall HER kinetics in both alkaline and neutral conditions. Furthermore, the 2D mesoporous structure provided abundant active sites and accessible channels for electron transfer and mass transport. Therefore, the Bi–Ni alloy exhibited high activity and stability for HER. Here, the Bi–Ni alloy required overpotentials of 56 mV and 183 mV at 10 mA cm^{-2} for HER under both alkaline and neutral conditions, respectively, which were close to that of commercial Pt/C in 1.0 M KOH and 1.0 M PBS (pH 7.0). The Bi–Ni alloy was further applied as a cathode and coupled with an IrO$_2$ anode for a full-cell in 1.0 M KOH. The required cell voltage was 1.53 V to drive 10 mA cm^{-2}, which was lower than that of the IrO$_2$‖Pt/C electrolyzer (1.64 V@10 mA cm^{-2}).

2. Experimental

2.1   Chemicals and reagents

Bismuth nitrate pentahydrate (Bi(NO$_3$)$_3$·5H$_2$O), disodium hydrogen phosphate dodecahydrate (Na$_2$HPO$_4$·12H$_2$O), potassium hydroxide (KOH), sodium phosphate monobasic dihydrate (NaH$_2$PO$_4$·2H$_2$O), and sodium hydroxide (NaOH) were acquired from Tianjin Damao Chemical Reagent Factory (China); glacial acetic acid (CH$_3$COOH), sodium hydrogen carbonate (NaHCO$_3$), and potassium iodide (KI) were purchased from Sinopharm (China); nickel sulfate heptahydrate (NiSO$_4$·7H$_2$O) was obtained from Xi'an Chemical Reagent Factory (China); Nafion solution was bought from Tianjin Incole Union Technology Co., Ltd (China); anhydrous sodium sulfate (Na$_2$SO$_4$) was acquired from Peking Chemical Reagent Company (China). All the reagents were used without any prior purification. DI water (18.25 MΩ cm) was used throughout the whole experiment process.

2.2   Preparation of BiOI precursor

The precursor BiOI nanosheets were synthesized according to the reference.[28] In short, 0.97 g of Bi(NO$_3$)$_3$·5H$_2$O was added to 20 mL of glacial acetic acid aqueous solution (1.2 M) and the mixture was vigorously stirred for 20 min until completely dissolved. Then, 5 mL of KI aqueous solution (2.0 M) was added to the above mixture in a dropwise fashion. Subsequently, the pH of the mixed solution was adjusted to 6.0 using 1.0 M NaOH aqueous solution. The resulting brick-red solution was then stirred for another 30 min before transferring it into a 50 mL Teflon-lined autoclave. Finally, it was treated at 160 °C for 2 h. The final brick-red BiOI precursor was obtained by centrifugation and washed four times with DI water.

2.3   Preparation of mesoporous Bi–Ni alloy nanosheets

The BiOI precursor was redispersed in 25 mL DI water. Four identical glassy carbon electrodes were prepared. Next, 5 μL of the dispersion liquid was dropped on each glassy carbon electrode (GCE), which will later be used as the working electrode. After natural drying, each working electrode was applied with 2 μL of 0.5% Nafion solution. To prepare four porous alloys samples (Bi$_{86.5}$Ni$_{13.5}$, Bi$_{84.8}$Ni$_{15.2}$, Bi$_{80.1}$Ni$_{19.9}$, Bi$_{76.2}$Ni$_{23.8}$), 15 cycles of CV in different concentrations of N$_2$-saturated NiSO$_4$ aqueous solution (0.01, 0.02, 0.03, and 0.04 M) were conducted within the potential window of −0.2 to −1.4 V *vs.* Ag/AgCl. During the reduction process, a graphite rod was used as the counter electrode. Afterwards, the working electrodes were removed and washed with DI water, followed by blow drying using nitrogen. Thus, the products of the mesoporous alloy were synthesized.

2.4   Characterizations

The data for the transmission electron microscopy (TEM), high-resolution transmission electron microscopy (HRTEM), energy dispersive X-ray spectroscopy (EDS), high angle annular dark field-scanning transmission electron microscopy (HAADF-STEM), and elemental mapping analyses for the samples were acquired using a TEM diffractometer (FEI Tecnai G2 F20) at 200 kV; scanning electron microscopy (SEM; Zeiss Sigma 300) was employed to obtain the morphologies of the catalysts; the crystal phases of the samples were obtained by X-ray diffraction (XRD; Smart Lab); the valence state of the elements on the surface of the samples was acquired by X-ray photoelectron spectrometry (XPS; Themofisher 250 XI); the atom ratio of the alloy was determined by inductively coupled plasma-optical emission spectrometry (ICP-OES; Agilent ICPOES 730); Brunauer–Emmett–Teller (BET) surface area experiments were conducted using a Micromeritics Surface Area analyzer (ASAP-2460); contact angle experiments were carried out on contact angle measuring instrument (SZ-CAMB3).

2.5   Electrochemical characterizations

The electrochemical performance data of the hydrogen evolution reaction (HER) and oxygen evolution reaction (OER) were collected from a standard three-electrode set-up using a CHI 760D electrochemical analyzer (Chenhua, Shanghai). The fresh electrocatalysts, graphite rod, and saturated calomel electrode (SCE) were adopted as the working electrodes, counter elec-

trode, and reference electrode, respectively. Polarization curves were conducted in a N_2-saturated 1.0 M electrolyte (PBS or KOH) at a scan rate of 5 mV s^{-1} with IR compensation. All the potentials were calculated with reference to the RHE (reversible hydrogen electrode) by adopting the formula: $E(V$ vs. RHE$) = E(V$ vs. SCE$) + 0.242 + 0.0592$pH. IR correction was obtained using the formula: $E_{corr} = E_{mea} - iR_S$ (where E_{corr} is the corrected potential, E_{mea} is the measured potential, and R_s is the electrolyte resistance). The R_s value was obtained from the x-intercept of the Nyquist plots in the high-frequency region, which was then used for IR correction. Cyclic voltammetry (CV) was conducted in a 0.1 V narrow potential window at different scan rates. The current density differences of the forward and reverse scans ($J_{anodic} - J_{cathodic}$) at 0.256 V vs. RHE (1.0 M PBS) and 0.441 V vs. RHE (1.0 M KOH) were plotted against the scan rates. The corresponding slope of the plot was two times the double-layer capacitance (C_{dl}). The C_{dl} was applied to calculate the electrochemically surface area (ECSA), while the ECSA was subsequently used to calculate the roughness factor of each sample (detailed calculation processes can be found in the ESI†). For the CV analysis, 1000 cycles of CV in the range of −0.5 to −0.8 V vs. SCE with a scan rate of 50 mV s^{-1} and i–t curves were used to measure the stability for hydrogen generation.

The overall water splitting performance of the Bi–Ni alloy was also investigated using the polarization curve obtained from the two-electrode set-up in 1.0 M KOH electrolyte, where the carbon paper (CP) supporting the Bi–Ni alloy was adopted as the cathode and anode. Prior to electrochemical deposition, the CP substrate (1 × 2 cm^2) was treated using acetone, ethanol, and deionized water followed by ultrasonic cleaning for 30 min. The $Bi_{84.8}Ni_{15.2}$ electrode was then obtained through the same electrochemical deposition method on the treated CP substrate (the coating area was 1.5 cm^2, and the side without the sample was sealed using transparent tape). The stability was investigated by performing an i–t study at a fixed potential. To better compare with noble metal catalysts, 20% Pt/C and IrO$_2$ catalysts on CP were prepared as follows: 20% Pt/C or IrO$_2$ catalyst (8.5 mg) was dispersed in 1 mL solution comprising 750 μL DI water and 250 μL ethanol by ultrasonic treatment for about 10 min. Next, 80 μL of the ink was coated on the CP surface. After air drying, 10 μL Nafion solution (0.5 wt%) was added to the catalyst surface, thus yielding two work-electrodes with a catalyst loading of 0.45 mg cm^{-2} (20% Pt/C or IrO$_2$).

2.6 DFT theoretical calculation

DFT was implemented in the Vienna *Ab initio* simulation package (VASP), which was adopted to optimize the geometric configuration for the Bi and Bi–Ni alloy.[29,30] Exchange–correlation interactions were represented using the generalized gradient approximation (GGA)[31] in the form of the Perdew–Burke–Ernzerhof functional (PBE).[32] A 500 eV cut-off energy for plain-wave basis sets was employed. The convergence thresholds for the energy and force were 10^{-5} eV and 5×10^{-3} eV Å^{-1} respectively. Adopting the experience correction of

Grimme's scheme,[33] the weak interaction was expressed through DFT+D3 ways. The vacuum space setting was greater than 20 Å, which was sufficient to prevent the interaction between periodic images. For the (110) surface, a four-layer structure with 3 × 3 × 1 K-point mesh was employed during the calculation. To mimic the real experimental ratio of Ni dopants, four and six Ni cluster structures were built and put on the Bi (110) surface for the $Bi_{80.1}Ni_{19.9}$ and $Bi_{84.8}Ni_{15.2}$ models to describe the catalytic interface of the samples. Norskov *et al.* proposed some descriptors, which were adopted to reflect the hydrogen-generation activity on the catalyst surface. Among the descriptors, ΔG_{H*} was a crucial parameter to determine the HER activity.[34] The change in the reaction's Gibbs free energy (ΔG) of each basic step was in view of the calculated hydrogen electrode model. It can be calculated with the formula

$$\Delta G = \Delta E + \Delta ZPE - T\Delta S$$

where ΔE is obtained directly from DFT calculations; ΔZPE is the change in zero-point energies, T is the temperature of 298.15 K, and ΔS is the change of entropy between the products and reactants.

3. Results and discussion

3.1 Characterization of the mesoporous Bi–Ni alloy nanosheets

Herein, mesoporous Bi–Ni alloy and Bi nanosheets were prepared by the electrochemical reduction of BiOI precursor in N_2-saturated $NiSO_4$ and Na_2SO_4 electrolyte, respectively. The synthesis procedure is illustrated in Scheme 1. Inductively coupled plasma-optical emission spectrometry (ICP-OES) analysis exhibited the atomic ratio of Bi to Ni for the four alloy samples (Table S1†). Thus, these four alloy products were named $Bi_{86.5}Ni_{13.5}$, $Bi_{84.8}Ni_{15.2}$, $Bi_{80.1}Ni_{19.9}$, and $Bi_{76.2}Ni_{23.8}$, respectively. The diffraction peaks of BiOI nanosheets were consistent with the tetragonal crystalline, corresponding to the standard card (PDF#10-0445) (Fig. S1a†). After electrochemical reduction, the diffraction peaks of $Bi_{84.8}Ni_{15.2}$ were slightly shifted relative to pure Bi (PDF#44-1246) and pure Ni (PDF#04-0850) (Fig. 1a). This confirmed the successful preparation of the alloy.[35,36] Furthermore, the smaller Ni atoms incorporated in the Bi lattice could induce lattice shrinkage and produce compressive lattice strain. Table S2† shows that the lattice strain of the $Bi_{84.8}Ni_{15.2}$ alloy was downregulated by 2.20% compared to pure Bi. Compressive strain in the Bi–Ni alloy could lead to a better interaction between the catalyst and the reactive intermediates of H and OH. Hence, the overall hydrogen-generation activity could be enhanced.[37]

The SEM image displayed a uniform and smooth nanosheets structure of the BiOI sample (Fig. S1b†). On the other hand, the $Bi_{84.8}Ni_{15.2}$ alloy comprised nanosheets with abundant mesopores, which can be seen from the SEM image in Fig. 1b. The average pore size was about 24.73 nm, which corresponded to the mesopore range. Additionally, the BET

Scheme 1 Illustration of the synthetic process for obtaining mesoporous Bi–Ni nanosheets.

surface area of the mesoporous $Bi_{84.8}Ni_{15.2}$ alloy was 43.49 m^2 g^{-1} (Fig. S2†). The high surface area of the $Bi_{84.8}Ni_{15.2}$ alloy could be attributed to the mesopores. Such a high surface area is beneficial for the exposure of more active sites, which in turn would support a desirable electrocatalytic performance. To explore the formation mechanism of the mesopores, various electrolyte solutions were investigated in the alloy preparation process. No pore to very few pores were observed on the nanosheets when $NaHCO_3$ or Na_2SO_4 aqueous solution was used as the electrolyte in the electrodeposition process (Fig. S3†). However, a large number of pores were formed when $NiSO_4$ aqueous solution was used as the electrolyte during electrodeposition (Fig. 1b). The formation of the pores may be attributed to the Kirkendall effect, where the pores are produced due to the different diffusion rates of Bi and Ni atoms during the electrochemical reduction process.[38]

The TEM images of $Bi_{84.8}Ni_{15.2}$ show that the alloy was made up of 2D nanosheets (Fig. 1c and d). From the high-resolution TEM (HRTEM) images of $Bi_{84.8}Ni_{15.2}$ alloy (Fig. 1e), the lattice spacing of the (110) crystal face was approximately 0.222 nm. Compared to the (110) crystal face of Bi (0.227 nm; Fig. S4†), the lattice spacing decreased when Ni atoms were incorporated. Hence, this demonstrated the existence of compressive strain in the $Bi_{84.8}Ni_{15.2}$ alloy, which was consistent with X-ray diffractometer (XRD) result. Furthermore, both the HAADF-STEM image (Fig. 1f) and EDS mapping images (Fig. 1g and h) showed that the Bi and Ni atoms were homogeneously distributed throughout the $Bi_{84.8}Ni_{15.2}$ surface. The EDS spectrum (Fig. S5a†) showed that the $Bi_{84.8}Ni_{15.2}$ consisted of Ni and Bi elements, while the Cu peak was ascribed to the copper base. The ratio of Bi to Ni was close to the ICP-OES analysis. The selected area electron diffraction (SAED) image showed that the $Bi_{84.8}Ni_{15.2}$ alloy was polycrystalline (Fig. 1i).

The Bi 4f spectrum presented the oxidation state of Bi^{3+} (164.3 and 159.0 eV) and metallic state of Bi^0 (156.9 and 162.2 eV).[39] The oxidation state (Bi^{3+}) may have arisen due to the exposure to air (Fig. 1j). The binding energies at 855.6 (Ni $2p_{3/2}$) and 873.2 eV (Ni $2p_{1/2}$), corresponding to satellite peaks of 861.2 and 879.7 eV in Fig. 1k, could be ascribed to the presence of Ni^{2+}, while the peaks at 874.8 and 856.8 eV belonged to the Ni^{3+}.[40] The Ni $2p_{3/2}$ signal of porous $Bi_{84.8}Ni_{15.2}$ alloy was deconvoluted into a peak at 852.6 eV, stemming from metallic Ni^0.[41,42] Furthermore, XPS analysis (Fig. S5b†) showed that the Bi^{3+} for the $Bi_{84.8}Ni_{15.2}$ alloy and $Bi_{80.1}Ni_{19.9}$ alloy peaks were shifted to lower binding energies compared with pure Bi. This phenomenon indicated the presence of electron transfer in the Bi–Ni alloy.[43] Meanwhile, the related description and characterization of the mesoporous $Bi_{80.1}Ni_{19.9}$ alloy are also provided in Fig. S6 and S7.†

3.2 Electrocatalytic HER of mesoporous Bi–Ni alloy nanosheets in alkaline electrolyte

As shown in Fig. 2a, the Bi nanosheet showed almost no activity, while Ni showed relatively weak activity. On the other hand, the mesoporous $Bi_{84.8}Ni_{15.2}$ alloy exhibited prominent HER activity, in which it only required an overpotential of 56 mV to reach a current density of 10 mA cm^{-2} in 1.0 M KOH. Note that the activity of $Bi_{84.8}Ni_{15.2}$ alloy towards HER was comparable to the benchmark 20% Pt/C. Moreover, the mesoporous $Bi_{84.8}Ni_{15.2}$ outperformed most reported bimetallic electrocatalysts (Table S3†). The high activity of $Bi_{84.8}Ni_{15.2}$ alloy could be attributed to the formation of abundant active sites,[44] numerous mesopores, and a compressive strain effect[31] on the surface of the catalyst. The effects of having different Ni contents in Bi–Ni alloy on the HER activity in alkaline electrolyte were also investigated (Fig. S8†). The alloy sample had a ratio of Bi to Ni of about 84.8/15.2, which presented the best
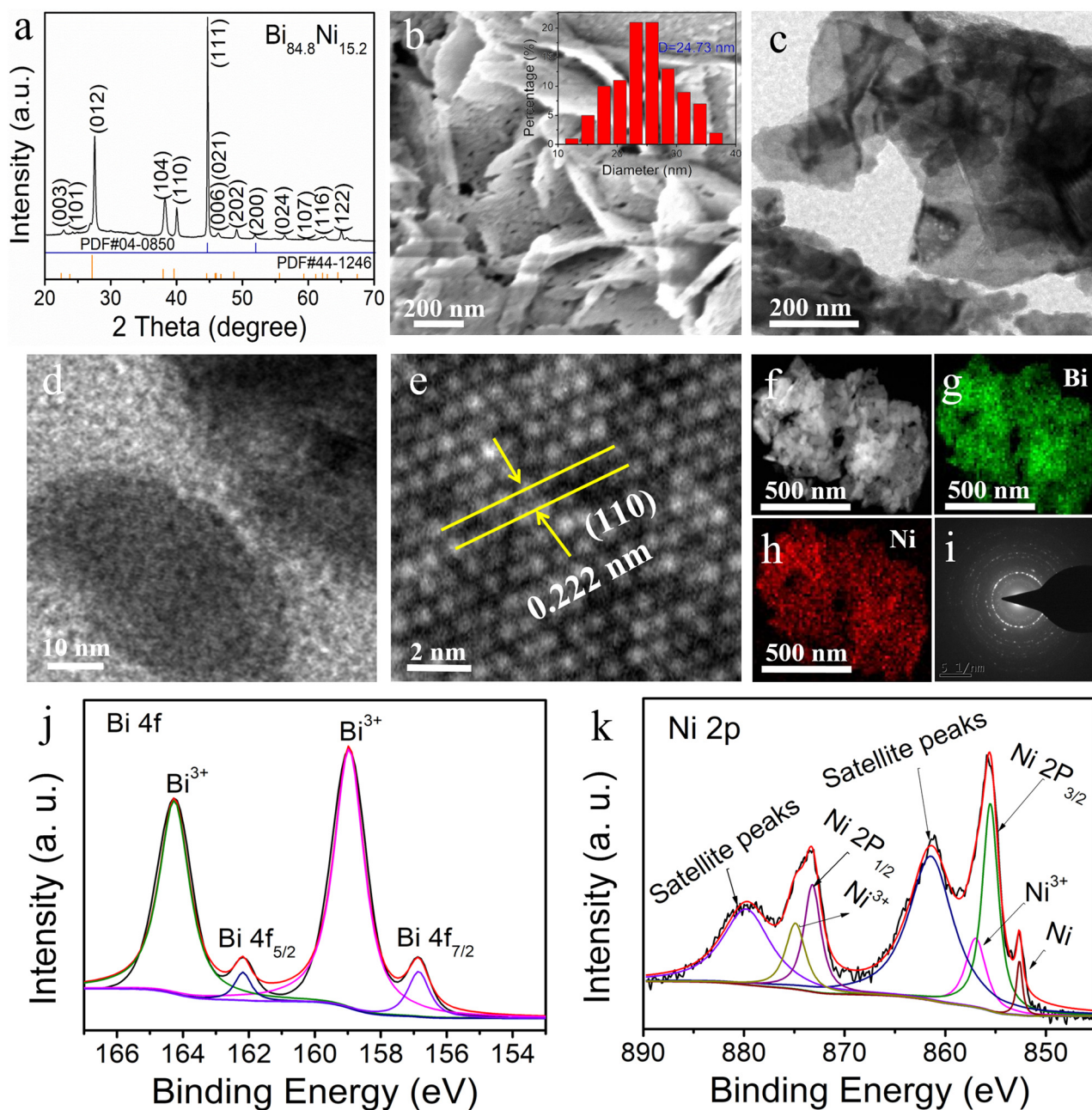
Fig. 1 Characterizations of mesoporous $Bi_{84.8}Ni_{15.2}$ alloy (a) XRD patterns; (b) SEM image; inset: pore-distribution image; (c and d) TEM images; (e) HRTEM image; (f) HAADF-STEM image; (g and h) EDS mapping images; (i) SAED pattern; (j) XPS spectrum of Bi 4f; (k) XPS spectrum of Ni 2p.

hydrogen-generation activity. Furthermore, the compressive strain of the alloy $Bi_{84.8}Ni_{15.2}$ was smaller than that of $Bi_{80.1}Ni_{19.9}$ (Bi to Ni ratio of 80.1 : 19.9) (Table S2 in the ESI†). The weak compression strain may lead to a strong interaction between the alloy electrocatalysts and the intermediate H and OH,[37] thus resulting in the high activity of $Bi_{84.8}Ni_{15.2}$ in alkaline media (Fig. S8 in the ESI†). Tafel slopes were acquired using the Tafel equation: $\eta = a + b \log|j|$ (where η is the applied overpotential, b is the Tafel slope, and j is the current density).[45] Fig. 2b shows that the Tafel slope of porous $Bi_{84.8}Ni_{15.2}$ alloy was 115 mV dec^{-1}, which was lower than that

of Ni (156 mV dec^{-1}). Thus, this indicated the rapid HER kinetics of $Bi_{84.8}Ni_{15.2}$ alloy and that the Volmer–Heyrovsky mechanism was followed during HER.[46] In Fig. 2c, the charge-transfer resistance (R_{ct}) of porous $Bi_{84.8}Ni_{15.2}$ alloy was 7.9 Ω, which was obviously smaller than those of Bi (1090.8 Ω) and Ni (38.6 Ω), thus indicating that the charge-transfer kinetics in the HER process was much faster. In addition, the electrochemical surface area (ECSA) is employed to estimate the intrinsic activity of electrocatalysts.[47] The double-layer capacitance (C_{dl}) values (Fig. 2d) were 13.65, 1.64, and 0.83 mF cm^{-2} for mesoporous $Bi_{84.8}Ni_{15.2}$ alloy, pure Ni, and pure Bi according to the
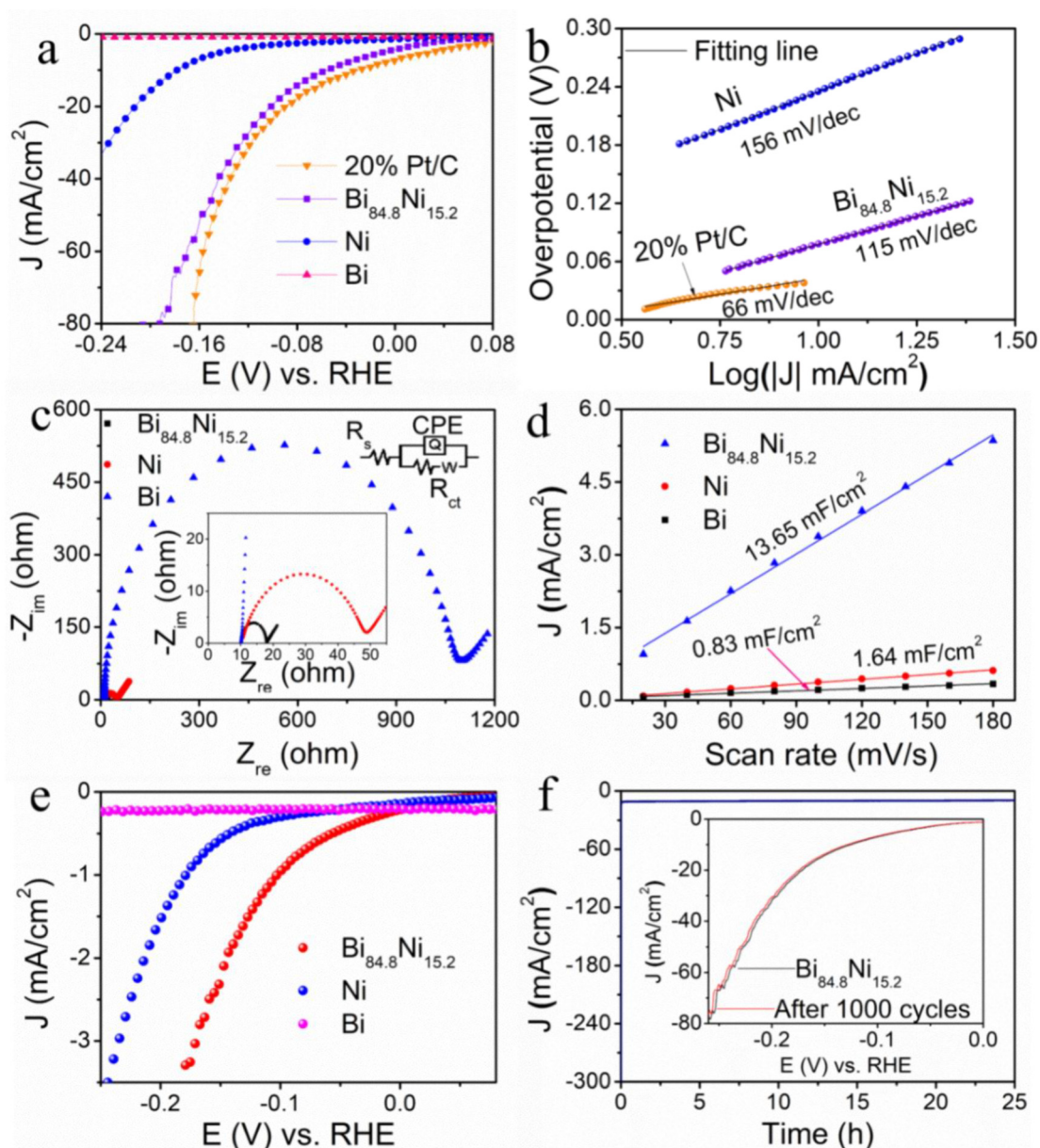
Fig. 2 (a) Polarization curves of samples for HER in 1.0 M KOH; (b) Tafel plots; (c) Nyquist plots at −56 mV *vs.* RHE. Inset shows the equivalent circuit; (d) capacitive current as a function of scan rate for the samples; (e) specific activity; (f) *I–t* test for $Bi_{84.8}Ni_{15.2}$ alloy at −56 mV *vs.* RHE; inset shows the polarization curves at 5 mV s^{-1} before and after 1000 cycles of CV.

above CVs (Fig. S9†). The corresponding ECSA values were 23.89, 2.87, and 1.45 cm^2 and the roughness factors (RF) were 341.29, 41.00, and 20.71 (calculation process in the ESI†). These results suggest that the mesoporous $Bi_{84.8}Ni_{15.2}$ alloy had a larger electrochemical active surface area and rough surface compared to pure Bi and pure Ni. The RF of the mesoporous $Bi_{84.8}Ni_{15.2}$ alloy was about 16 times more than that of the Bi nanosheets, which was ascribed to the formation of abundant mesopores. Additionally, the catalytic efficiency of the obtained samples was evaluated by normalization of the raw current using the ECSA. As shown in Fig. 2e, the mesoporous $Bi_{84.8}Ni_{15.2}$ showed the best catalytic efficiency for HER.

With the increase in overpotential, the turnover frequency (TOF) value of mesoporous $Bi_{84.8}Ni_{15.2}$ alloy was higher than that of pure Ni. This suggested a higher catalytic efficiency of mesoporous $Bi_{84.8}Ni_{15.2}$ alloy during the HER process (Fig. S10a†). Furthermore, the contact angles data in Fig. S11† present that $Bi_{84.8}Ni_{15.2}$ and $Bi_{80.1}Ni_{19.9}$ alloys and Bi nanosheets had angles of about 63°, 75.5°, and 90° after water-drop diffusion at the same time, respectively. These results demonstrate that the hydrophilicity of Bi–Ni alloy was significantly higher than pure Bi, which is conducive for the adsorption of H_2O molecules. The contact angle of $Bi_{84.8}Ni_{15.2}$ alloy was smaller than that of $Bi_{80.1}Ni_{19.9}$ alloy. This phenom-

enon may be caused by the higher oxophilicity of $Bi_{84.8}Ni_{15.2}$ alloy than that of $Bi_{80.1}Ni_{19.9}$ alloy. The above-mentioned facts clearly indicate that the excellent catalytic activity of Bi–Ni alloys may be attributed to the mesoporous 2D nanosheet structure and the alloy effect.

Stability is also an essential criterion for the practical application of a catalyst. In Fig. 2f, the mesoporous $Bi_{84.8}Ni_{15.2}$ alloy still maintained its initial current density for 25 h or 1000 cycles of CV electrolysis. Both the morphology and lattice spacing corresponding to the (110) crystal face of the mesoporous $Bi_{84.8}Ni_{15.2}$ alloy (Fig. S12a–c†) could still be observed after the long-term electrolysis. In Fig. S12d,† all the XRD peaks of the mesoporous $Bi_{84.8}Ni_{15.2}$ alloy remained unchanged after electrolysis, and no new peaks appeared. The high-resolution XPS analysis (Fig. S12e and f†) also revealed the chemical states of Ni and Bi did not change after continuous electrolysis. All the above results suggest that mesoporous $Bi_{84.8}Ni_{15.2}$ alloy has outstanding HER stability in alkaline electrolyte.

3.3 Electrocatalytic HER of mesoporous Bi–Ni alloy nanosheets in neutral electrolyte

Fig. 3a clearly shows that the mesoporous $Bi_{80.1}Ni_{19.9}$ alloy needed a lower overpotential (183 mV $vs.$ RHE@10 mA cm^{-2}) than pure Bi and pure Ni, while the activity was inferior to mercantile 20% Pt/C. Furthermore, the HER activities of the Bi–Ni alloys with different Ni contents were also investigated in a neutral medium (Fig. S13†), in which mesoporous $Bi_{80.1}Ni_{19.9}$ alloy exhibited the optimal activity. The Tafel slope of mesoporous $Bi_{80.1}Ni_{19.9}$ alloy was 141 mV dec^{-1} (Fig. 3b), which indicated faster kinetic characteristics than pure Ni (165 mV dec^{-1}).[48,49] The mesoporous $Bi_{80.1}Ni_{19.9}$ alloy had the lowest R_{ct} (Fig. 3c), and this suggested that the mesopores and the Ni incorporation into the Bi lattice are conducive for the enhancement of the charge-transfer kinetics of $Bi_{80.1}Ni_{19.9}$ alloy towards HER. The C_{dl} values in Fig. 3d were obtained using CVs (Fig. S14†) at variable scanning rates.[50] The ECSA values of mesoporous $Bi_{80.1}Ni_{19.9}$ alloy, pure Ni, and pure Bi were calculated to be 27.04, 15.31, and 1.24 cm^2, respectively, and the corresponding RF values were also calculated to be 386.29, 218.71, and 17.71 (ESI†). The high ECSA and RF of $Bi_{80.1}Ni_{19.9}$ alloy may be attributed to the abundant mesopores on the surface of the alloy, which is good for exposing more active sites, thus enhancing the HER activity. The specific activity in Fig. 3e shows that the mesoporous $Bi_{80.1}Ni_{19.9}$ alloy presented the best intrinsic catalytic activity. In Fig. S10b,† the TOF value of mesoporous $Bi_{80.1}Ni_{19.9}$ alloy was higher than that of pure Ni, which suggests that the mesoporous $Bi_{80.1}Ni_{19.9}$ alloy had higher catalytic efficiency than pure Ni in 1.0 M PBS (pH 7.0) for HER.

In Fig. 3f, it can be seen that the mesoporous $Bi_{80.1}Ni_{19.9}$ catalyst could preserve its activity during the 20 h electrolysis or 1000 cycles of CV. The morphology of $Bi_{80.1}Ni_{19.9}$ alloy was also retained after long-term electrolysis, as exhibited in Fig. S15a and b.† The lattice spacing of $Bi_{80.1}Ni_{19.9}$ alloy corresponding to the (110) crystal face remained unchanged

(Fig. S15c†), and the polycrystalline property of the mesoporous $Bi_{80.1}Ni_{19.9}$ alloy still existed (Fig. S15d†). Also, the phase of $Bi_{80.1}Ni_{19.9}$ alloy remained unchanged during electrolysis which was evident in the XRD patterns (Fig. S15e†). The EDS spectrum (Fig. S15f†) also showed that mesoporous $Bi_{80.1}Ni_{19.9}$ alloy still had the same elements before and after electrolysis. All the above results indicate that the mesoporous $Bi_{80.1}Ni_{19.9}$ alloy has excellent stability in neutral electrolyte for HER.

3.4 Mechanism of mesoporous Bi–Ni alloy nanosheets towards HER

To understand the mechanism of Bi–Ni alloys on the HER activity, DFT was adopted to calculate the Gibbs free energy of each step for HER in neutral and alkaline conditions. The Bi (110) and Bi–Ni alloy (110) surfaces were used for the catalysts' theoretical models (Fig. S16†). The optimal structures at each reaction stage of Bi, $Bi_{84.8}Ni_{15.2}$, and $Bi_{80.1}Ni_{19.9}$ are shown in Fig. 4a. The Gibbs free energy of each step for HER in neutral and alkaline conditions are displayed in Fig. 4b. The dissociation energies of a water molecule on $Bi_{80.1}Ni_{19.9}$ and $Bi_{84.8}Ni_{15.2}$ surfaces were 0.23 and 0.03 eV, respectively, which were obviously smaller than that of pure Bi (1.27 eV). This shows that Ni alloying plays a crucial role in accelerating H_2O dissociation and improving H* formation. Regardless of the mechanistic route, the HER always entails the formation of $M–H^*$ intermediates. Theoretically, the closer it is to zero $|\Delta G_{H^*}|$, the higher the HER activity. A large and negative ΔG_{H^*} value represents a strong binding of H with the catalyst. The H* is firmly adsorbed on the catalyst surface. However, as H* is difficult to release from the catalyst surface, this hinders the subsequent process of the H_2 generation. Conversely, a large and positive ΔG_{H^*} value indicates a weak adsorption of H on the catalyst surface, which limits the conversion rate of the H*.[51,52] Therefore, $\Delta G_{H^*} \approx 0$ implies an optimal adsorption and desorption balance between the catalyst surface and H. The H* could be converted to H_2 on the $Bi_{80.1}Ni_{19.9}$ and $Bi_{84.8}Ni_{15.2}$ alloy surfaces, with obtained ΔG_{H^*} values of only -0.07 and -0.26 eV, respectively, which were lower than for the Bi nanosheets (0.54 eV). Here, due to the unique oxophilicity of the local positive charged and unfilled d-orbital of the Ni ions produced by the oxidation of Ni, the OH from the dissociation of water molecules prefer to adsorb on the surface Ni sites.[53] Meanwhile, the H prefer to adsorb on Bi sites due to the comparable electronegativity.[54] Consequently, the dissociation step of water molecules is accelerated (Volmer step: $H_2O + e^- = H^* + OH^-$). The generated OH^- desorbs from the surface Ni sites and enters the electrolyte solution. Then, one H* can recombine with one H_2O molecule and one electron to produce H_2 at the adjacent surface Ni atom (Heyrovsky step: $H_2O + e^- + H^* = H_2 + OH^-$). This is because the electrons are transferred from Bi atom to Ni atom (Fig. 4c, Fig. S17a,† and Fig. 4d). It can be concluded that the alloying effect can regulate the electronic structure of the catalyst surface, thus facilitating the dissociation of a water H_2O molecule and optimized ΔG_{H^*}. The ΔG_{H^*} values of $Bi_{84.8}Ni_{15.2}$ and $Bi_{80.1}Ni_{19.9}$ were
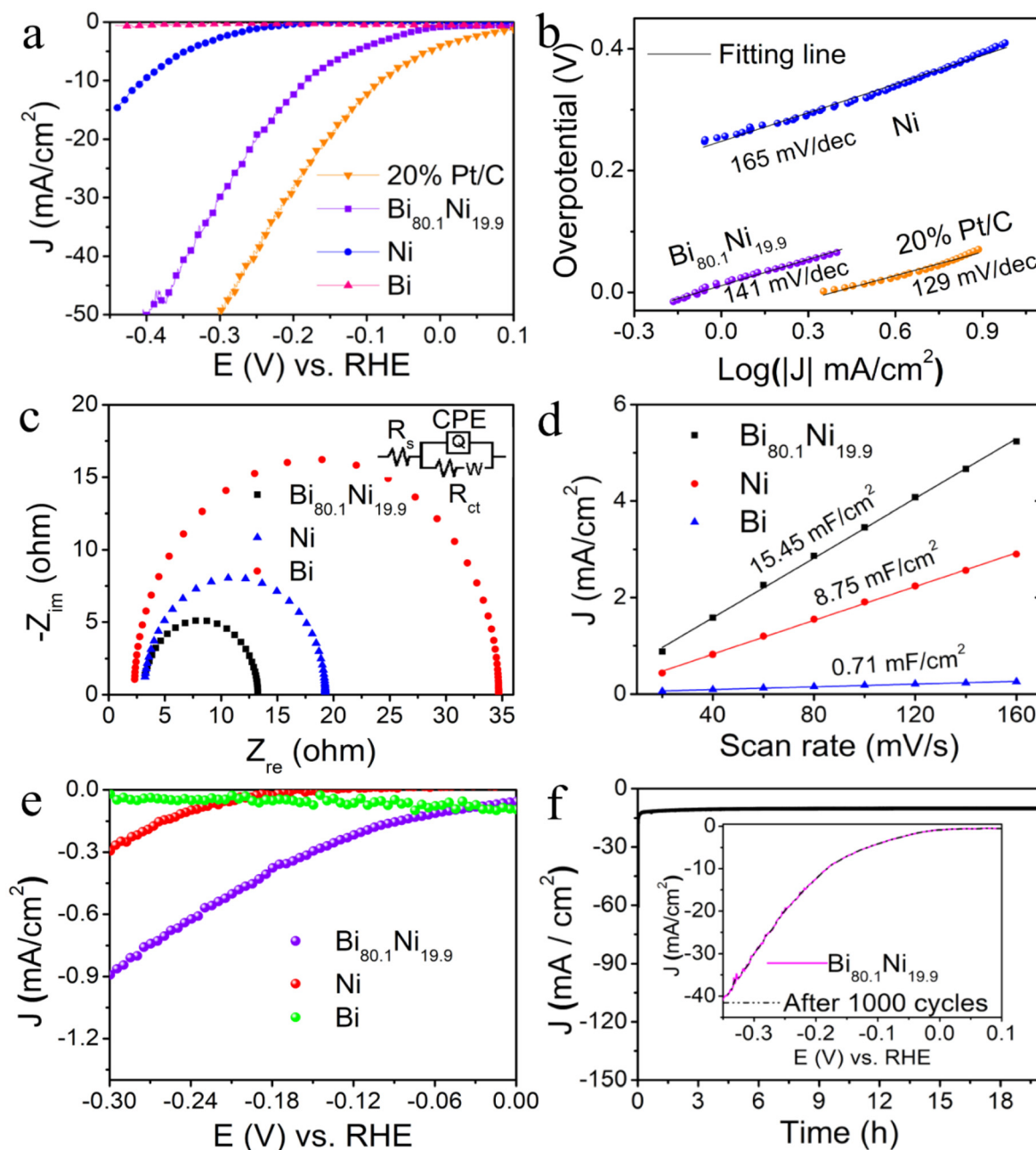
Fig. 3 (a) Polarization curves for HER in 1.0 M PBS (pH 7.0); (b) Tafel plots; (c) Nyquist plots at −183 mV *vs.* RHE. Inset shows the equivalent circuit; (d) capacitive current as a function of scan rate for the samples; (e) specific activity; (f) *I*−*t* test for Bi$_{80.1}$Ni$_{19.9}$ alloy at −183 mV *vs.* RHE; inset shows the polarization curves at 5 mV s^{-1} before and after 1000 cycles CV.

different, which suggested the content of Ni has a considerable influence on the HER activity (Fig. S8 and S13†).

The density of states (DOS; Fig. 4e) indicated that the d-band centre of Ni was shifted upward on Bi$_{84.8}$Ni$_{15.2}$ and Bi$_{80.1}$Ni$_{19.9}$ compared with pure Bi, suggesting Ni had a more electron-rich state. Meanwhile, in Fig. S17b–d,† compared with pure Bi, the DOS of Bi$_{84.8}$Ni$_{15.2}$ and Bi$_{80.1}$Ni$_{19.9}$ alloys orbital increased a lot at the Fermi level, resulting in more free electrons on the Ni sites. This phenomenon not only enhanced the metallic character and electrical conductivity of Bi–Ni alloy

but also decreased the excessive binding effect of H on alloy surface, which boosted the HER activity.[55] These results were consistent with the EIS analysis (Fig. 2c and 3c) and polarization curves (Fig. 2a and 3a).

3.5 Electrocatalytic overall water splitting performance of mesoporous Bi–Ni alloy

Driven by the exciting HER activity of mesoporous Bi$_{84.8}$Ni$_{15.2}$ alloy, a two-electrode water splitting full-cell (Fig. 5a) was constructed using Bi$_{84.8}$Ni$_{15.2}$ alloy as the cathode and IrO$_2$ as the
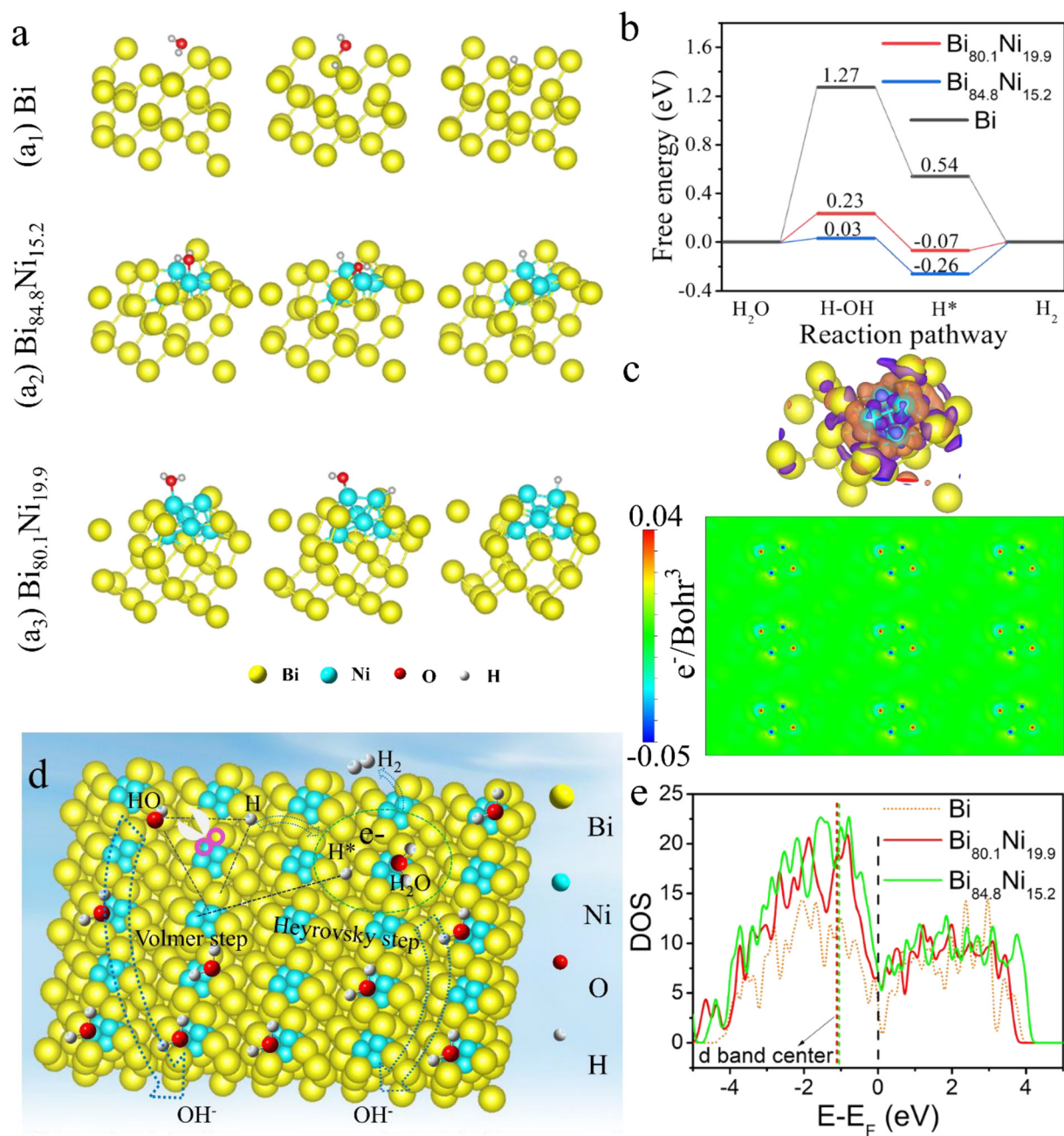
Fig. 4 (a) Optimized structures at different reaction stages; (b) Gibbs free energy of HER; (c) Top: Electron transfer in $Bi_{80.1}Ni_{19.9}$. Colour: Yellow, Bi; cyan, Ni; orange and purple isosurfaces represent electron accumulation and electron depletion at an isosurface cut-off of 0.002 e^- per Bohr^3. Bottom: Electron density change plots of $Bi_{80.1}Ni_{19.9}$; (d) schematic diagram of Bi−Ni alloy towards HER. (e) DOS of pure Bi, and $Bi_{80.1}Ni_{19.9}$ and $Bi_{84.8}Ni_{15.2}$ alloys; Fermi level indicated by the black dashed line.

anode in 1.0 M KOH ($IrO_2\|Bi_{84.8}Ni_{15.2}$). This exhibited a lower voltage (1.53 V@10 mA cm^{-2}) than $IrO_2\|Pt/C$ (1.64 V @10 mA cm^{-2}) (Fig. 5b) because of the rapid kinetics and bubble-diffusion procedures (inset of Fig. 5c and video S1†). The higher activity of $IrO_2\|Bi_{84.8}Ni_{15.2}$ was possibly due to the stronger oxophilicity of Ni, which was caused by the local positive charged and unfilled d-orbital of the Ni ions.[53,56] The OH from the dissociation of water molecules prefer to adsorb on the surface Ni sites, which makes it easy to accelerate the dis-

sociation of water molecules in the alkaline media. Thus, the $IrO_2\|Bi_{84.8}Ni_{15.2}$ system needed a low cell voltage of 1.53 V at the current density of 10 mA cm^{-2} in 1.0 M KOH. The oxygen evolution reaction (OER) performance of $Bi_{84.8}Ni_{15.2}$ alloy was further studied in 1.0 M solutions (PBS [pH 7.0] and KOH). The detailed information and relevant figures (Fig. S18–S22†) can be found in the ESI.† The results indicate that the real active substance Bi_2O_3/β-NiOOH possessed the best OER activity, with an overpotential of 479 mV@50 mA cm^{-2} and a
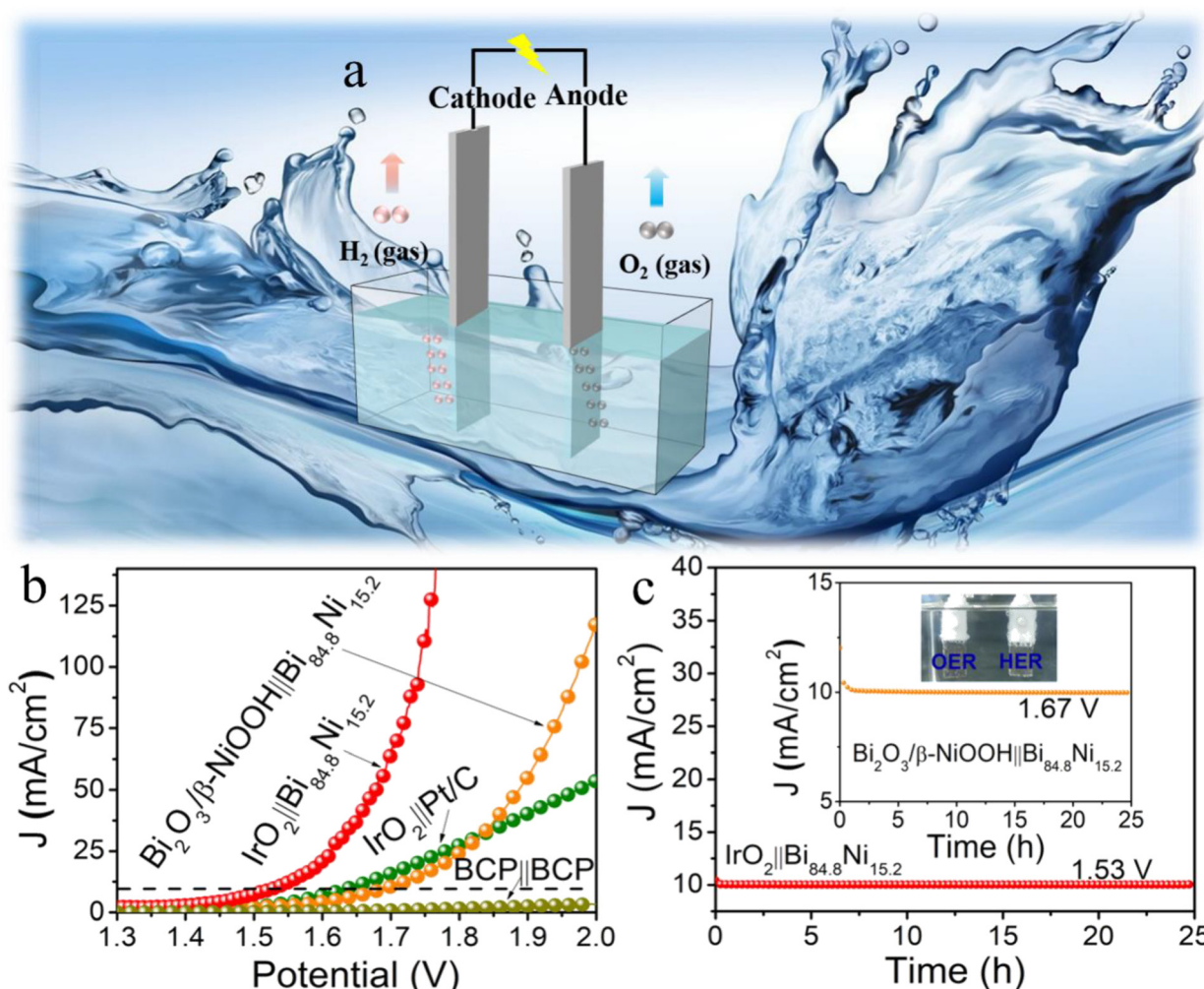
Fig. 5 Overall water splitting performance (a) two-electrode device; (b) polarization curves at a scan rate of 5 mV s^{-1}; (c) I–t curves at an invariant cell voltage; Inset: image taken during water splitting.

low Tafel slope of 74 mV dec^{-1} in 1.0 M KOH (Fig. S19a and b†). The overall water splitting of Bi$_2$O$_3$/β-NiOOH‖Bi$_{84.8}$Ni$_{15.2}$ electrolyzer needed 1.67 V cell voltage to reach a current density of 10 mA cm^{-2} (Fig. 5b). The current density for water electrolysis using the IrO$_2$‖Bi$_{84.8}$Ni$_{15.2}$ system outperformed that of Bi$_2$O$_3$/β-NiOOH‖Bi$_{84.8}$Ni$_{15.2}$ at the cell voltage of 1.5–2.0 V. This performance could be explained as follows. As shown in Fig. S19a (ESI†), the current response of Bi$_2$O$_3$/β-NiOOH was produced by both the water oxidation and the oxidation of Bi$_{84.8}$Ni$_{15.2}$ to Bi$_2$O$_3$/β-NiOOH at 1.6–1.8 V (*vs.* RHE). While using IrO$_2$ as the anode, the current was only generated by the water oxidation. The Bi$_{84.8}$Ni$_{15.2}$ oxidation occurred at the cell voltage of 1.13 V in the two-electrode system (Bi$_2$O$_3$/β-NiOOH‖Bi$_{84.8}$Ni$_{15.2}$ pair) (Fig. S19e, ESI†). However, the current was provided only by the water oxidation at the cell voltage of 1.5–2.0 V. Thus, the current response of the electrolysis system (IrO$_2$‖Bi$_{84.8}$Ni$_{15.2}$) was higher than that of Bi$_2$O$_3$/β-NiOOH‖Bi$_{84.8}$Ni$_{15.2}$ at the cell voltage of 1.5–2.0 V.

Durability is also a key criterion for evaluating an electrolytic cell.[57] The constant current response of IrO$_2$‖Bi$_{84.8}$Ni$_{15.2}$

and Bi$_2$O$_3$/β-NiOOH‖Bi$_{84.8}$Ni$_{15.2}$ electrolyzers were examined by recording i–t tests for 25 h electrolysis in the same electrolyte (Fig. 5c). However, the current density of IrO$_2$‖Pt/C declined significantly with the prolongation of time (Fig. S23†). This result is in agreement with the reported literature.[58]

4. Conclusions

In summary, as-fabricated 2D porous Bi–Ni alloy displayed a high intrinsic HER activity under both alkaline and neutral conditions, as well as exceptional long-time stability over 20 h of continuous electrolysis. DFT showed that the alloying effect reduced the ΔG_{H*} value and also increased the electron density near the Fermi level of the Bi–Ni alloy. The alloying effect between Bi and Ni regulated the electronic structure, thus improving the intrinsic activity of Bi–Ni catalyst. The activity of IrO$_2$‖Bi$_{84.8}$Ni$_{15.2}$ towards overall water splitting also outperformed the commercial IrO$_2$‖Pt/C. This work shows that the incorporation of Ni element into the Bi-based catalyst

could significantly boost the HER performance, which will be conducive for the development of economical and efficient electrocatalysts for energy conversion.

Conflicts of interest

The authors declare that there is no competing financial interest.

Acknowledgements

References

1 T. H. Wang, L. Tao, X. R. Zhu, C. Chen, W. Chen, S. Q. Du, Y. Y. Zhou, B. Zhou, D. D. Wang, C. Xie, P. Long, W. Li, Y. Y. Wang, R. Chen, Y. Q. Zou, X. Z. Fu, Y. F. Li, X. F. Duan and S. Y. Wang, *Nat. Catal.*, 2021, **5**, 66–73.

2 R. Subbaraman, D. Tripkovic, K. C. Chang, D. Strmcnik, A. P. Paulikas, P. Hirunsit, M. Chan, J. Greeley, V. Stamenkovic and N. M. Markovic, *Nat. Mater.*, 2012, **11**, 550–557.

3 C. L. Hu, L. Zhang and J. L. Gong, *Energy Environ. Sci.*, 2019, **12**, 2620–2645.

4 J. D. Holladay, J. Hu, D. L. King and Y. Wang, *Catal. Today*, 2009, **139**, 244–260.

5 C. T. Dinh, A. Jain, F. P. G. de Arquer, P. De Luna, J. Li, N. Wang, X. L. Zheng, J. Cai, B. Z. Gregory, O. Voznyy, B. Zhang, M. Liu, D. Sinton, E. J. Crumlin and E. H. Sargent, *Nat. Energy*, 2019, **4**, 107–114.

6 J. Staszak-Jirkovsky, C. D. Malliakas, P. P. Lopes, N. Danilovic, S. S. Kota, K. C. Chang, B. Genorio, D. Strmcnik, V. R. Stamenkovic, M. G. Kanatzidis and N. M. Markovic, *Nat. Mater.*, 2016, **15**, 197–203.

7 J. M. Wei, M. Zhou, A. C. Long, Y. M. Xue, H. B. Liao, C. Wei and Z. C. J. Xu, *Nano-Micro Lett.*, 2018, **10**, 75–89.

8 N. Han, Y. Wang, H. Yang, J. Deng, J. H. Wu, Y. F. Li and Y. G. Li, *Nat. Commun.*, 2018, **9**, 1320.

9 J. Greeley, T. F. Jaramillo, J. Bonde, I. B. Chorkendorff and J. K. Norskov, *Nat. Mater.*, 2006, **5**, 909–913.

10 X. Q. Mu, J. N. Gu, F. Y. Feng, Z. Y. Xiao, C. Y. Chen, S. L. Liu and S. C. Mu, *Adv. Sci.*, 2021, **8**, 2002341.

11 H. J. Huang, D. S. Yu, F. Hu, S. C. Huang, J. N. Song, H. Y. Chen, L. L. Li and S. J. Peng, *Angew. Chem., Int. Ed.*, 2022, **61**, 202116068.

12 Y. Wang, B. Kong, D. Y. Zhao, H. T. Wang and C. Selomulya, *Nano Today*, 2017, **15**, 26–55.

13 F. Lv, B. Huang, J. Feng, W. Zhang, K. Wang, N. Li, J. Zhou, P. Zhou, W. Yang, Y. Du, D. Su and S. Guo, *Natl. Sci. Rev.*, 2021, **8**, nwab019.

14 J. N. Song, S. Y. Qiu, F. Hu, Y. H. Ding, S. L. Han, L. L. Li, H. Y. Chen, X. P. Han, C. H. Sun and S. J. Peng, *Adv. Funct. Mater.*, 2021, **31**, 2100618.

15 J. Zhang, T. Wang, P. Liu, Z. Q. Liao, S. H. Liu, X. D. Zhuang, M. W. Chen, E. Zschech and X. L. Feng, *Nat. Commun.*, 2017, **8**, 15437.

16 P. M. Csernica, J. R. McKone, C. R. Mulzer, W. R. Dichtel, H. D. Abruna and F. J. DiSalvo, *ACS Catal*, 2017, **7**, 3375–3383.

17 Z. X. Li, C. C. Yu, Y. Y. Wen, Y. Gao, X. F. Xing, Z. T. Wei, H. Sun, Y. W. Zhang and W. Y. Song, *ACS Catal.*, 2019, **9**, 5084–5095.

18 H. L. S. Santos, P. G. Corradini, M. Medina, J. A. Dias and L. H. Mascaro, *ACS Appl. Mater. Interfaces*, 2020, **12**, 17492–17501.

19 Y. Ito, T. Ohto, D. Hojo, M. Wakisaka, Y. Nagata, L. H. Chen, K. L. Hu, M. Izumi, J. Fujita and T. Adschiri, *ACS Catal.*, 2018, **8**, 3579–3586.

20 Z. W. Seh, J. Kibsgaard, C. F. Dickens, I. B. Chorkendorff, J. K. Norskov and T. F. Jaramillo, *Science*, 2017, **355**, 146–159.

21 L. L. Li, D. S. Yu, P. Li, H. J. Huang, D. Y. Xie, C. C. Lin, F. Hu, H. Y. Chen and S. J. Peng, *Energy Environ. Sci.*, 2021, **14**, 6419–6427.

22 H. Y. Jin, J. Wang, D. F. Su, Z. Z. Wei, Z. F. Pang and Y. Wang, *J. Am. Chem. Soc.*, 2015, **137**, 2688–2694.

23 J. Pan, S. Yu, Z. Jing, Q. Zhou, Y. Dong, X. Lou and F. Xia, *Small Struct.*, 2021, 2100076.

24 Q. Q. Pan, C. Y. Xu, X. Li, J. F. Zhang, X. L. Hu, Y. Geng and Z. M. Su, *Chem. Eng. J.*, 2021, **405**, 126962.

25 B. N. Khiarak, M. Hasanzadeh and A. Simchi, *Inorg. Chem. Commun.*, 2021, **127**, 108525.

26 X. G. Feng, X. J. Bo and L. P. Guo, *J. Power Sources*, 2018, **389**, 249–259.

27 K. Lan, Y. Liu, W. Zhang, Y. Liu, A. Elzatahry, R. C. Wang, Y. Y. Xia, D. Al-Dhayan, N. F. Zheng and D. Y. Zhao, *J. Am. Chem. Soc.*, 2018, **140**, 4135–4143.

28 N. Han, Y. Wang, H. Yang, J. Deng, J. H. Wu, Y. F. Li and Y. G. Li, *Nat. Commun.*, 2018, **9**, 1320–1327.

29 G. Kresse and J. Furthmiiller, *Comput. Mater. Sci.*, 1996, **6**, 15–50.

30 G. Kresse, *Phys. Rev. B: Condens. Matter Mater. Phys.*, 1996, **54**, 11169–11186.

31 J. P. Perdew, K. Burke and M. Ernzerhof, *Phys. Rev. Lett.*, 1996, **77**, 3865–3868.

32 J. P. Perdew, M. Ernzerhof and K. Burke, *J. Chem. Phys.*, 1996, **105**, 9982–9985.

33 S. Grimme, *J. Comput. Chem.*, 2006, **27**, 1787–1799.

34 C. Wei, Y. M. Sun, G. G. Scherer, A. C. Fisher, M. Sherburne, J. W. Ager and Z. C. J. Xu, *J. Am. Chem. Soc.*, 2020, **142**, 7765–7775.

35 G. R. Chen, X. T. Yang, Z. X. Xie, F. L. Zhao, Z. Y. Zhou and Q. Yuan, *J. Colloid Interface Sci.*, 2020, **562**, 244–251.

36 F. Shen, Y. M. Wang, G. F. Qian, W. Chen, W. J. Jiang, L. Luo and S. B. Yin, *Appl. Catal., B*, 2020, **278**, 119327.

37 X. S. Wang, Y. H. Zhu, A. Vasileff, Y. Jiao, S. M. Chen, L. Song, B. Zheng, Y. Zheng and S. Z. Qiao, *ACS Energy Lett.*, 2018, **3**, 1198–1204.

38 J. C. Li, C. Zhang, T. Zhang, Z. H. Shen, Q. W. Zhou, J. Pu, H. J. Ma, T. H. Wang, H. G. Zhang, H. M. Fan, Y. Y. Wang and H. X. Ma, *Chem. Eng. J.*, 2020, **397**, 125457.

39 Z. Khazaee, A. R. Mahjoub and A. H. C. Khavar, *Appl. Catal., B*, 2021, **297**, 120480.

40 M. J. Qu, Y. M. Jiang, M. Yang, S. Liu, Q. F. Guo, W. Shen, M. Li and R. X. He, *Appl. Catal., B*, 2020, **263**, 118324.

41 A. A. Dubale, Y. Y. Zheng, H. L. Wang, R. Hubner, Y. Li, J. Yang, J. W. Zhang, N. K. Sethi, L. Q. He, Z. K. Zheng and W. Liu, *Angew. Chem., Int. Ed.*, 2020, **59**, 13891–13899.

42 C. H. Wang, H. C. Yang, Y. J. Zhang and Q. B. Wang, *Angew. Chem., Int. Ed.*, 2019, **58**, 6099–6103.

43 M. F. Sanad, A. R. Puente Santiago, S. A. Tolba, M. A. Ahsan, O. Fernandez-Delgado, M. ShawkyAdly, E. M. Hashem, M. MahrousAbodouh, M. S. El-Shall, S. T. Sreenivasan, N. K. Allam and L. Echegoyen, *J. Am. Chem. Soc.*, 2021, **143**, 4064–4073.

44 F. L. Zhao, J. Y. Ye, Q. Yuan, X. T. Yang and Z. Y. Zhou, *J. Mater. Chem. A*, 2020, **8**, 11564–11572.

45 Y. G. Li, H. L. Wang, L. M. Xie, Y. Y. Liang, G. S. Hong and H. J. Dai, *J. Am. Chem. Soc.*, 2011, **133**, 7296–7299.

46 C. J. Lei, Y. Wang, Y. Hou, P. Liu, J. Yang, T. Zhang, X. D. Zhuang, M. W. Chen, B. Yang, L. C. Lei, C. Yuan, M. Qiu and X. L. Feng, *Energy Environ. Sci.*, 2019, **12**, 149–156.

47 K. Zhan, C. H. Feng, X. T. Feng, D. Zhao, S. Yue, Y. J. Li, Q. Z. Jiao, H. S. Li and Y. Zhao, *ACS Sustainable Chem. Eng.*, 2020, **8**, 6273–6281.

48 M. A. Ahsan, A. R. P. Santiago, Y. Hong, N. Zhang, M. Cano, E. Rodriguez-Castellon, L. Echegoyen, S. T. Sreenivasan and J. C. Noveron, *J. Am. Chem. Soc.*, 2020, **142**, 14688–14701.

49 Q. Zhang, D. F. Yan, Z. Z. Nie, X. B. Qiu, S. Y. Wang, J. M. Yuan, D. W. Su, G. X. Wang and Z. J. Wu, *ACS Appl. Energy Mater.*, 2018, **1**, 571–579.

50 S. F. Fu, C. Z. Zhu, J. H. Song, M. H. Engelhard, X. L. Li, D. Du and Y. H. Lin, *ACS Energy Lett.*, 2016, **1**, 792–796.

51 H. Y. Li, S. M. Chen, H. F. Lin, X. B. Xu, H. Z. Yang, L. Song and X. Wang, *Small*, 2017, **13**, 1701487.

52 S. Shen, Z. Lin, K. Song, Z. Wang, L. Huang, L. Yan, F. Meng, Q. Zhang, L. Gu and W. Zhong, *Angew. Chem., Int. Ed.*, 2021, **60**, 12360–12365.

53 M. Gong, W. Zhou, M. C. Tsai, J. G. Zhou, M. Y. Guan, M. C. Lin, B. Zhang, Y. F. Hu, D. Y. Wang, J. Yang, S. J. Pennycook, B. J. Hwang and H. J. Dai, *Nat. Commun.*, 2014, **5**, 5695.

54 S. B. Pillai, S. D. Dabhi and P. K. Jha, *Int. J. Hydrogen Energy*, 2018, **43**, 21649.

55 X. Mu, J. Gu, F. Feng, Z. Xiao, C. Chen, S. Liu and S. Mu, *Adv. Sci.*, 2021, **8**, 2002341.

56 B. Ruqia and S. I. Choi, *ChemSusChem*, 2018, **11**, 2643–2653.

57 M. S. Balogun, W. T. Qiu, H. Yang, W. J. Fan, Y. C. Huang, P. P. Fang, G. R. Li, H. B. Ji and Y. X. Tong, *Energy Environ. Sci.*, 2016, **9**, 3411–3416.

58 B. H. R. Suryanto, Y. Wang, R. K. Hocking, W. Adamson and C. Zhao, *Nat. Commun.*, 2019, **10**, 2041–1723.